Stress-induced morphological instabilities at the nanoscale examined using the phase field crystal approach

Kuo-An Wu and Peter W. Voorhees
Department of Materials Science and Engineering, Northwestern University, Evanston, Illinois 60208, USA
(Received 19 May 2009; published 11 September 2009)

The stress-induced morphological instability of an interface is examined with the recently developed phase field crystal (PFC) approach. Our results show that the interface width, generally assumed to be zero thickness in classical theory, is a crucial length scale for phenomena at the nanoscale. We find that the critical wavenumber of the instability deviates from the prediction of the continuum theory when the length scale of the instability is on the order of the interface width. In addition, we find that large stresses induce nonlinear elastic effects that alter both the wavelength of the instability and the interfacial morphology. This nonlinear elastic effect is generic and thus will be observable during heteroepitaxy. Finally, we show that the diffusional dynamics employed in the PFC model can capture quantitatively the stress field that accompanies the diffusional evolution of interfaces.

DOI: 10.1103/PhysRevB.80.125408 PACS number(s): 61.46.−w, 68.08.−p, 68.55.−a

I. INTRODUCTION

The morphological stability of strained thin films has been extensively investigated due to its importance in the growth of self-assembled nanostructures. The planar surface of a uniaxially stressed solid is unstable with respect to perturbations having a wavelength greater than a critical value as a result of the Asaro-Tiller-Grinfeld (ATG) instability.[1–5] In classical theory, this critical wavelength is related to the ratio of the surface energy to the elastic strain energy density as thus scales as the square of the applied strain. Recent work by Huang and Elder suggests a different scaling relation between the critical wavelength and the applied strain for large strains as a result of dislocation formation.[6] Furthermore, as evolution continues, both experiments and theoretical analyses show that the surface develops smooth low-curvature peaks and high-curvature grooves. In continuum calculations these grooves deepen and eventually form a cusp singularity.[7–11] In experiments, however, prior to the appearance of the singularity dislocations form.[12] Experiment also shows that the stability of a thin film can depend on the sign of the applied strain, in contradiction to classical continuum theory where the stability of a film is independent of the sign of the applied strain.[13] Explanations of this phenomena involve the difference in surface diffusivity of the atoms in an alloy film.[14,15]

Various approaches have been employed to model the ATG instability. The phase field method has been employed but the model cannot capture the physics of dislocation formation at deep grooves, the manner in which nanoscale islands develop, and nonlinear elastic phenomena associated with the large strains that are applied in experiment.[16–18] A combined phase field-dislocation field analysis can account for dislocation formation, but since it is a continuum model requires large length scales and employs linear elasticity.[19] Recently, the phase field crystal (PFC) method has been developed as an alternative approach to model elastic and plastic deformations in crystals on atomistic length scales, and on a time scale that is much larger than molecular dynamics (MD) simulations.[20–23] The free-energy functional used in the PFC can be found using classical density functional theory (DFT),[22,24] and many interface properties are realistic and comparable to those found in MD simulations.[24] However, it is not clear that the PFC model can describe phenomena such as the ATG instability, since the dynamics is strictly diffusional. Such dynamics can lead to nonphysical behavior when the processes of interest are driven by stress.[25]

We show that the evolution of the ATG instability is strongly influenced by the atomic nature of crystals in the large strain limit that is typically employed in experiment. Specifically for stressed solids in contact with a fluid, such as in liquid-phase epitaxy, the thickness of the solid-liquid interface increases the size scale of the instability. In addition, large stresses lead to nonlinear elastic effects that alter the interfacial morphology, as well as the wavelength and strain dependence of the instability. This nonlinear elastic effect is generic and thus will be present when a stressed solid is in contact with a vapor phase or vacuum. We also identify the reasons why a PFC model that employs strictly diffusional dynamics can reproduce the predictions of continuum theory, which assumes a completely relaxed strain field, in the small stress limit.

II. BASIC EQUATIONS AND SCALING

We consider the PFC model defined by the free-energy functional[20,21]

$$F = \int d\mathbf{r}\left\{\frac{\phi}{2}[a + \lambda(q_0^2 + \nabla^2)^2]\phi + g\frac{\phi^4}{4}\right\}. \quad (1)$$

The order parameter ϕ is the density field measured from a constant reference value, and q_o is the wavenumber which sets the length scale of lattice planes to be $2\pi/q_o$. The parameters a and λ determine the shape of the polynomial approximation of the liquid structure factor $S(K)$ in the PFC model. They were fixed in previous studies to match either the liquid phase compressibility and the bulk modulus,[21,22] or the solid-liquid interface properties.[24] By defining the parameter $\delta = -a/(\lambda q_o^4)$, and making the substitutions,

$$q_0\vec{\mathbf{r}} \rightarrow \vec{r}, \tag{2}$$

$$\sqrt{\frac{g}{\lambda q_0^4}}\phi \rightarrow \psi, \tag{3}$$

$$\frac{g}{\lambda^2 q_0^6}F \rightarrow \mathcal{F}, \tag{4}$$

we obtain the following dimensionless free-energy functional:

$$\mathcal{F} = \int d\vec{r}\left\{\psi[-\delta + (\nabla^2+1)^2]\frac{\psi}{2} + \frac{\psi^4}{4}\right\}. \tag{5}$$

The control parameter δ is associated with the interface thickness $\mathcal{W} \sim \delta^{-1/2}$. The parameters are chosen to yield a hexagonal crystal in equilibrium with a liquid. Assuming relaxational dynamics the evolution equation for a conserved order parameter is

$$\frac{\partial \phi}{\partial \tau} = \Gamma\nabla^2\frac{\delta F}{\delta \phi}, \tag{6}$$

where Γ is a phenomenological constant that is related to a diffusion coefficient.[21] The dimensionless evolution equation becomes

$$\frac{\partial \psi}{\partial t} = \nabla^2[-\delta\psi + (\nabla^2+1)^2\psi + \psi^3], \tag{7}$$

where the dimensionless time $t=\Gamma\lambda q_o^6\tau$.

III. SIMULATION METHOD

We set $\delta=0.1$, and thus the interface thickness $\mathcal{W}$ is similar to the solid-liquid interface thickness of Fe,[24] about 10 Å, if we employ the wavenumber from the liquid structure of Fe, $q_o \approx 2.985$ Å^{-1}. The hexagonal lattice density can be approximated by considering the contribution of the principal reciprocal lattice vectors,

$$\psi(\vec{r}) \approx \bar{\psi} + \sum_i A_i e^{i\vec{K}_i\cdot\vec{r}} = \bar{\psi} + 2A\left(2\cos\frac{qx}{2}\cos\frac{\sqrt{3}qy}{2} + \cos qx\right), \tag{8}$$

where $\bar{\psi}$ is the average density, q is the magnitude of the principal reciprocal lattice vectors ($q=|\vec{K}_i|$), and A is the amplitude of density wave. The parameters A and q are computed by substituting Eq. (8) into Eq. (5) and minimizing the resulting free-energy with respect to A and q, which yields

$$A = -\frac{1}{5}\bar{\psi} + \frac{1}{15}\sqrt{15\delta - 36\bar{\psi}^2} \tag{9}$$

and $q=1$.

However, for finite values of δ the lattice parameter $(2\pi/q)$ of the stress-free hexagonal lattice is slightly expanded due to the nonlinear coupling of the principal reciprocal lattice vectors to higher order reciprocal lattice vectors. Although the expansion of the lattice parameter is small for the above simulation parameters, it turns out to be essential to account for this small difference, since the applied strains are also small in the linear elasticity regime. The expansion of the lattice parameter is computed using a two-mode approximation where the second mode is the set of vectors formed by combining two vectors with the angle $\pi/3$ between them from the principal reciprocal lattice vectors,

$$\psi(\vec{r}) = \bar{\psi} + 2A_1\left(2\cos\frac{q'x}{2}\cos\frac{\sqrt{3}q'y}{2} + \cos q'x\right) + 2A_2\left(2\cos\frac{3q'x}{2}\cos\frac{\sqrt{3}q'y}{2} + \cos\sqrt{3}q'y\right), \tag{10}$$

where the amplitudes A_1, A_2, and the wavenumber q' are solved with the free-energy minimization procedure as described above. The free-energy minimization calculation is performed at the coexistence solid density, $\bar{\psi}=-0.196$, that is obtained from the equilibrium solid-liquid system in PFC simulations. The wavenumber q' is about 0.045% smaller than that obtained from the one-mode approximation. The PFC simulations gives a similar value $\Delta q/q=(q-q')/q = 0.047\%$ that is used in the following simulations as the stress-free reference state to give more accurate results.

To model a solid stressed in the x direction that is in contact with liquid, we set the simulation parameters in two dimensions to be $(\Delta x, \Delta y)=[(1+\epsilon_{xx})\pi/(4q'), \pi/(3\sqrt{3})]$ on a system of size $N_x\Delta x \times N_y\Delta y$ with periodic boundary conditions, where ϵ_{xx}, N_x, and N_y are the uniaxial applied strain and the number of grid points in the x, y dimension, respectively.

We employ parameters that yield a strained hexagonal lattice of the form,

$$\psi(\vec{r}) = \bar{\psi}_s + 2A_s\left(2\cos\frac{q'x}{2(1+\epsilon_{xx})}\cos\frac{\sqrt{3}q'y}{2(1-\epsilon_{xx}/3)} + \cos\frac{q'x}{(1+\epsilon_{xx})}\right), \tag{11}$$

which occupies the region $N_y\Delta y/8 < y < 7N_y\Delta y/8$ with two planar surfaces that are in contact with the liquid, $\psi(\vec{r})=\bar{\psi}_l$, which occupies the rest of the system. $\bar{\psi}_s$ and $\bar{\psi}_l$ are the coexistence density of solid and liquid, respectively, and the solid amplitude A_s is approximated by Eq. (9). A reference system with stable planar interfaces is obtained by running a system of size 16 by 3072 meshpoints in x and y, respectively, until it reaches equilibrium. The coexistence densities $\bar{\psi}_s$ and $\bar{\psi}_l$ are measured from the reference system. We find that the coexistence densities weakly depend on applied strain. For example, for 2.5% compressive strain the coexistence densities change by less than 0.5%. To investigate the stability of the planar surface for different wavelengths, systems with different N_x are constructed by repeating this smaller simulation laterally. Additionally, small random fluctuations covering eight to ten atom layers across the upper solid-liquid interfaces is applied initially to trigger the instability, if it is present.

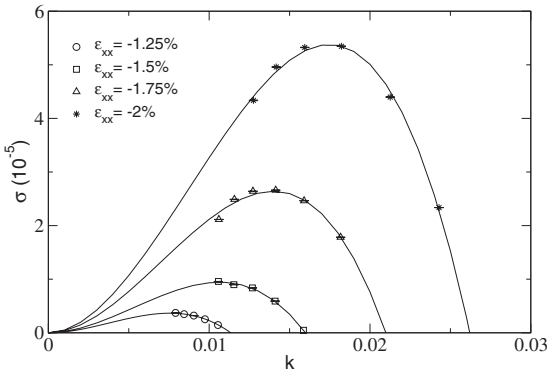

FIG. 1. Measured linear growth rate as a function of the wavenumber for different values of applied strains. The dispersion relation is consistent with the bulk diffusion mechanism (solid lines). k_c is given by $\sigma(k_c)=0$.

IV. RESULTS AND ANALYSIS

A. Surface kinetics

There are different possible mass transport mechanisms during surface evolution: surface diffusion, bulk diffusion, and evaporation/condensation. The mass transport process controls the maximally unstable mode and the rate at which the instability occurs.[3–5,26] To investigate the mass transport mechanism in the PFC model, we compute the growth rates by tracking the amplitude of a perturbation of the solid-liquid interface with a wavelength that is equal to the lateral dimension of the simulation box. The interface positions are not well defined from the density plot in the PFC model due to decay of the periodic density field into the liquid. In order to extract the interface positions, we calculate the coarse-grained free-energy density which is the average of the free-energy density over one unit cell area to obtain a nonoscillating but smooth free-energy density profile. The interface positions are then determined by finding locations where the coarse-grained free-energy density equals the average of the free-energy density of solid and liquid.

We determine the growth rate of the perturbation with an amplitude that is sufficiently small that the perturbation evolves as $h(x,t)=h_o \exp(\sigma t)$, where σ is the growth rate and h_o is the initial amplitude of the perturbation. Figure 1 plots the growth rate of surface undulations as a function of the wave number for different compressive strains. From Fig. 1, we see that the data fit the predictions of linear theory where the amplitude evolves by bulk diffusion, $\sigma(k)=\mathcal{D}(Ak^2-Bk^3)$, where $\mathcal{D}$, A, and B are related to the diffusion constant, elastic strain energy and surface energy, respectively. For tensile strains, the same dispersion relation of bulk diffusion is observed. However, the maximally unstable mode, $k_m=2A/3B$, is smaller under tensile strains than compressive strains for the same magnitude of the applied strains employed in Fig. 1. The asymmetry of the maximally unstable mode is due to the asymmetry of the elastic energy resulted from the higher order terms in the elastic energy portion of the free energy, which is discussed later. Although the PFC model does not exclude other diffusion processes, given the fit shown in Fig. 1 it is expected that the bulk diffusion process is the dominant mass transport mechanism for all strains examined.

B. Elastic relaxation

The evolution equation of the PFC model, Eq. (7), describes the diffusion of the conserved density field ψ at the time scale associated with the diffusion constant Γ. Linear elasticity is included by the presence of the gradient terms in the free energy, which give rise to an increase in the free energy that scales as the strain squared under small applied strains.[21] Both diffusion and elastic relaxation processes needed to model the stress-induced instability are thus incorporated in the PFC model. However, it is not clear from the evolution equation how fast the stress fields relax. To model the stress-induced instability, which occurs at a diffusional time scale, the elastic stress fields must relax faster than the density field to ensure the system is always at mechanical equilibrium during surface evolution. To determine if this is the case, we derive the strain fields from the classical elasticity theory using linear perturbation theory and compare them with those found in the PFC.

We assume a uniaxially stressed semi-infinite solid ($y<0$) that is in contact with liquid ($y>0$) in two dimensions and linear isotropic elasticity. The stress and strain fields in the unperturbed state, corresponding to a planar surface, are

$$\bar{\sigma}_{xx} = \frac{E}{1+\nu}\left(\bar{\epsilon}_{xx} + \frac{\nu}{1-\nu}(\bar{\epsilon}_{xx} + \bar{\epsilon}_{yy})\right),$$

$$\bar{\sigma}_{yy} = 0, \quad \bar{\epsilon}_{xx} = \epsilon_{xx},$$

$$\bar{\epsilon}_{yy} = \frac{1}{E}(\bar{\sigma}_{yy} - \nu\bar{\sigma}_{xx}), \tag{12}$$

where E is Young's modulus and ν is Poisson's ratio. The small surface perturbation at the surface $y=0$ has the form of $\hat{h}\Phi(x)$, where $\hat{h}$ is the amplitude of the perturbation, and $\Phi(x)$ is the normal mode $\Phi(x)=\exp(ikx)$. The perturbed states can be expressed as

$$h = \hat{h}\Phi(x),$$

$$\sigma_{ij} = \bar{\sigma}_{ij} + \hat{\sigma}_{ij}(y)\Phi(x),$$

$$\epsilon_{ij} = \bar{\epsilon}_{ij} + \hat{\epsilon}_{ij}(y)\Phi(x), \tag{13}$$

where $\hat{\sigma}_{ij}$ and $\hat{\epsilon}_{ij}$ are magnitudes of perturbed stress and strain fields, respectively. Assuming the system is at mechanical equilibrium, $\nabla\cdot\sigma=0$, and the boundary condition that the perturbation in the stress decays to zero in the solid and zero pressure in the liquid, we obtain

$$\hat{\epsilon}_{xx}(x,y) = -k\hat{h}\epsilon_{xx}[2+(1+\nu)ky]\exp(ky)\Phi(x),$$

$$\hat{\epsilon}_{yy}(x,y) = k\hat{h}\epsilon_{xx}[2\nu+(1+\nu)ky]\exp(ky)\Phi(x). \tag{14}$$

To compute the strain fields in the PFC simulations, an accurate determination in positions of density peaks is

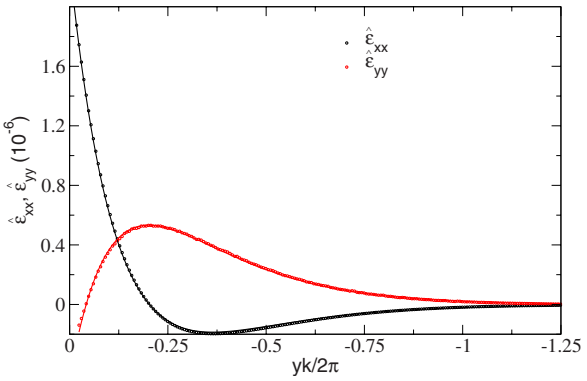

FIG. 2. (Color online) The perturbed strain fields calculated from the PFC model and the linear stability analysis derived in Eq. (14) are plotted in dots and solid lines, respectively, for a compressive strain $\epsilon_{xx}=-1.047\%$ (dots) along the y axis which goes through the peak of the surface perturbation.

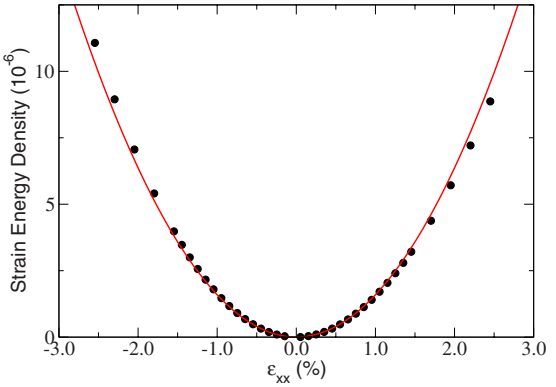

FIG. 3. (Color online) Elastic strain energy density calculated from the PFC simulations (solid circles) and linear elasticity theory $\mathcal{E}=1/2E\epsilon_{xx}^2$ (red line) as a function of applied strains. The Young's modulus used in the linear elasticity calculation is obtained by linearly interpolating Young's modulus at $\epsilon_{xx}=0$ in Fig. 4.

needed. The location of density peaks is determined numerically by requiring the density field to satisfy the condition that $\nabla\psi=0$ at peaks. The strain fields in the PFC simulations are obtained by computing the spatial variation in positions of density peaks relative to the unstrained reference system. The perturbed strain fields are then the difference in strain fields found for the perturbed and unperturbed cases. We compute the perturbed strain fields as close as possible to the solid-liquid interface that still yields reasonable strain fields. In the PFC simulations, it is difficult to determine accurately the interface position and the magnitude of the surface perturbation that correspond to the sharp interface limit given in the linear perturbation theory, so we determine these values by fitting to the $\hat{\epsilon}_{xx}$ plot, and hold these fixed when making comparisons to all components of the strain tensor. Figure 2 shows that the perturbed strain fields, taken from the peak of the surface profile, calculated from the PFC simulation that is subjected to the applied strain $\epsilon_{xx}=-1.047\%$ during the evolution of the instability; the system size in the x dimension is approximately 20 nm if we assume a lattice parameter to be 2.985 Å and $\nu=1/3$ (which is the case for hexagonal lattices when the amplitudes of density waves of the higher order reciprocal lattice vectors are small). The simulation results are in remarkably good agreement with the linear perturbation theory. We find similar agreement at other times during the evolution of the instability, as long as the interfacial perturbation remains small. This suggests that, for the above simulation parameters, the elastic fields in the PFC model relax much faster than the density field, despite the presence of only one time scale in the diffusional dynamics of Eq. (7). Thus on the time scale of the interfacial evolution, the solid in the PFC model is always in mechanical equilibrium for the above simulation parameters. This is because elastically induced strains are associated with small changes in the location of the maxima of the density field, which depend on the amplitudes of density waves rather than the average density. Elastic relaxation is then achieved by the local phase changes in amplitudes of density waves. The elastic relaxation process is thus governed by the amplitudes of density waves which are nonconserved order parameters. On the contrary, the mass diffusion process, that determines the interfacial evolution, is governed by conserved dynamics which typically happens on a much slower time scale than the nonconserved dynamics. This idea is also consistent with recent multiscale analyses of the PFC model[6,27] where the amplitudes and the density evolve in the nonconserved and conserved fashion, respectively.

C. Critical wavenumber

For small perturbations in the interfacial morphology, continuum theory predicts that the critical wavenumber is given by $k_c=4\mathcal{E}/\gamma$, where $\mathcal{E}=\frac{1}{2}E\epsilon_{xx}^2$ is the elastic strain energy density of a crystal with a uniaxial strain ϵ_{xx}, and γ is the interfacial energy per unit length. The elastic strain energy density $\mathcal{E}$ is obtained as the difference in the free-energy density between the stressed state and the stress-free state, which is calculated numerically for different applied strains using the corresponding coexistence solid density. Linear elasticity predicts that for the uniaxially stressed solid considered the elastic energy should be independent of the sign of the applied strain. The dependence of the elastic strain energy density on the applied strain is plotted in Fig. 3. We find a very small variation in the strain energy with the sign of the applied strain, about 6% for strains less than 1%. We are thus confident that for strains less than 1% linear elasticity holds. However, for example, for 2% strains of opposite signs the strain energy changes by 12%. The asymmetry of the elastic energy results from the higher order terms in the strain, that are naturally present in the PFC free energy, which change sign for opposite strains, as detailed in Appendix B. This asymmetry of the elastic energy suggests strain-dependent elastic constants and the onset of nonlinear elasticity which is discussed later. Figure 4 plots the strain-dependent Young's modulus, $E=2\mathcal{E}/\epsilon_{xx}^2$. The linear dependence of Young's modulus on strains suggests that the leading order term in nonlinear elasticity is cubic which is consistent with the elastic energy calculation derived in Eq. (B2).

The surface energy is determined using the method described in Ref. 24. The interfacial energy dependence on the applied strain is plotted in Fig. 5. For a strain of 2% the

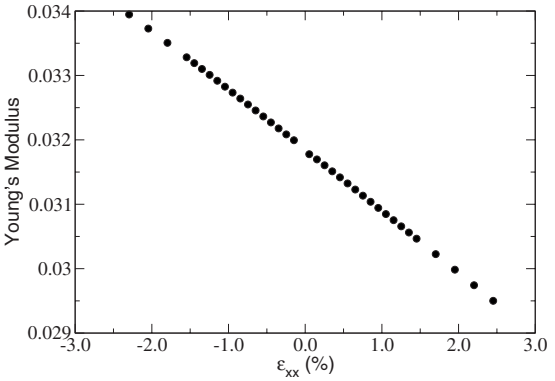

FIG. 4. The strain-dependent Young's modulus calculated from the PFC model, $E \equiv 2\mathcal{E}/\epsilon_{xx}^2$.

interfacial energy changes by 0.6%, thus the interfacial stress is very small.

The theoretical critical wavenumber, $k_c = 4\mathcal{E}/\gamma$, is computed employing the elastic energy $\mathcal{E}$ and the interfacial energy γ from Figs. 3 and 5, respectively, yielding the solid lines in Fig. 6. The theoretical critical wavenumber is compared to that found in the PFC simulations (see Fig. 6). The critical wavenumbers computed from the PFC model are in good agreement with the continuum theory when the applied strains are less than 1.25%. k_c is roughly independent of the sign of the applied strain and it increases with strain as ϵ_{xx}^2. Thus the PFC can capture realistically the predictions of continuum theory when the instability occurs on sufficiently large length scales and the strains are sufficiently small.

However this is not the case for strains exceeding 1.25%, where k_c depends on the sign of the strain and is not proportional to ϵ_{xx}^2. There are two physical phenomena that are responsible for this—the nonlinear elasticity and finite interface thickness. As discussed above, the difference between the critical wavenumbers for tensile and compressive strains is due to nonlinear elasticity. The difference of the critical wavenumber between the tensile and compressive case at a given strain is nearly equal to the difference of the critical wavenumber of the simulation data, indicating that nonlinear elasticity is playing an important role in the evolution of the instability at large strains. A similar dependence on the sign of the applied strain has been observed experimentally in

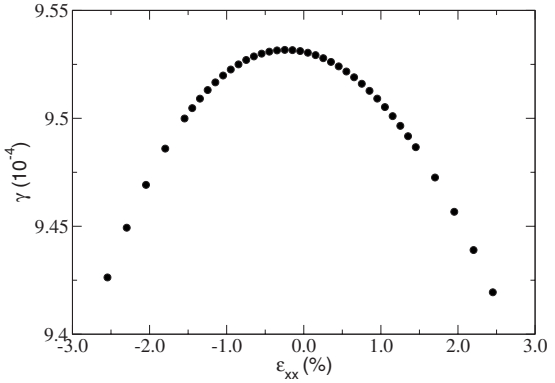

FIG. 5. The interfacial energy γ calculated from the PFC model as a function of applied strains.

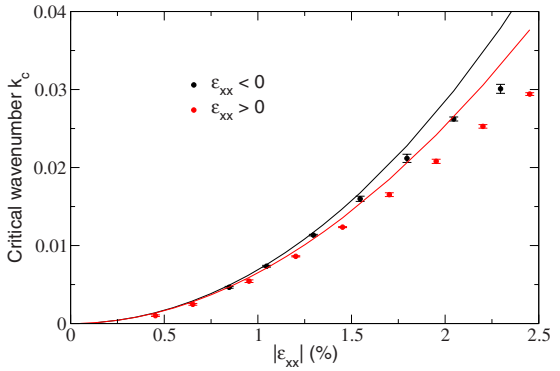

FIG. 6. (Color online) Comparison of critical wavenumbers obtained from the PFC model for compressive strains (black circles) and tensile strains (red circles), and the corresponding linear stability analysis $k_c = 4\mathcal{E}/\gamma$ (solid lines). The critical wavenumber for tensile strains is smaller than the critical wavenumber for compressive strains at large strains due to nonlinear elasticity.

$Ge_{0.5}Si_{0.5}$ alloy, where the film is stable under a 2% tensile strain while it becomes rough under compressive strains exceeding 1.4%.[13]

Despite the nonlinear elasticity, the critical wavenumber of the simulations is smaller than the theoretical prediction at large strains. When the magnitude of the strain is large, λ_c is sufficiently small that it is on the order of the interface thickness. Continuum theory rests on the assumption that the solid and liquid are separated by a sharp interface, while in reality, and the PFC model, the interface thickness is nonzero. The interface thickness in this case is about 15% of λ_c for $k_c \approx 0.03$. Due to the finite interface thickness every physical quantity changes smoothly across the interface, including the elastic constants. The elastic strain energy shown in Eq. (B2) is a function of the amplitude of density waves that decays smoothly into liquid in the interfacial region. The elastic strain energy in the interfacial region is thus smaller than in the bulk solid and therefore the elastic energy is smaller than that assumed in continuum theory. As a result, k_c found in the PFC is smaller than that given by continuum theory at large strains, but agrees with classical theory for small strains. Furthermore, as shown in Eq. (14), the perturbed strain fields decay at the length scale equal to the wavelength of the instability, thus the interface thickness becomes more important when the ratio of the wavelength of the instability to the interface thickness becomes smaller. It is shown in Fig. 6 that the deviation of the critical wavenumber from classical theory is larger at large strains where the critical wavelength becomes smaller. The interface thickness does not vary with the sign of ϵ_{xx} and thus is responsible for the decrease in the critical wavenumber for both tensile and compressive strains.

To further establish that the critical wavenumber is modified by the finite interface thickness we examine the case with a smaller value of $\delta = 0.01$ (i.e., a thicker interface thickness $\mathcal{W} \approx 30$ Å). We reduce the applied strain to 0.75% for which the nonlinear elasticity is negligible, but $\mathcal{W}/\lambda \approx 15\%$. As expected we find a 30% deviation in the critical wavenumber from the classical theory even though the strains are small. This deviation is consistent with previous results.

Therefore the PFC shows that for perturbations along the solid-liquid interface of Fe with wavelengths on the order of

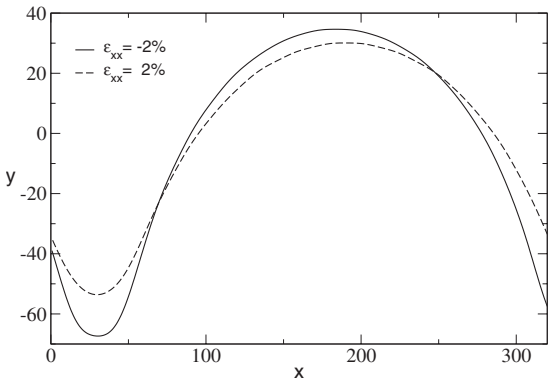

FIG. 7. The nonlinear shapes of the surface evolution. The steady states of the systems with the same number of atoms in the x dimension (N_x=400) under 2% compression (solid line) and tension (dashed line), respectively.

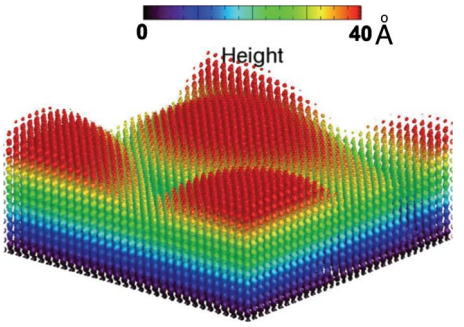

FIG. 8. (Color online) The surface evolution of a biaxially strained solid in three dimensions as determined using the PFC model. Height is in the unit of Angstrom with the parameter q_o =2.985 Å^{-1}.

10 nm the interface thickness will alter the wavelength of the instability. This requires large strains, however, on the order of 2%. Nevertheless, such strains may be attainable in materials in which dislocation motion and formation is more difficult, such as Si. Since the solid-liquid interface thickness in Si is on the same order as Fe, we expect this change in the wavelength due to the interface thickness to be present in Si as well.

D. Nonlinear elasticity controlled surface morphology

As the amplitude of the perturbation in the interfacial morphology grows, for systems with a lateral dimension slightly larger than the critical wavelength λ_c, the surface profiles reach steady states somewhat similar to those found in Refs. 10 and 11, specifically interfaces with rounded peaks and sharp troughs (see Fig. 7). However, due to the large strain concentration at the troughs and the significant deviation in the strain from the applied stress at the peaks that accompany the development of strongly nonplanar interfaces, the morphologies depend on the sign of ϵ_{xx} unlike in the simulations based upon linear elasticity.[10] In this case the interfacial morphologies of the same crystal under 2% applied strains of the opposite sign are different in the height and curvatures at the peak and valley, and show clearly the strong influence of nonlinear elasticity on the development of highly nonplanar interfaces. The difference between these shapes is not related to the interface thickness since the ratio of the system dimension to the interface thickness is approximately the same. This is consistent with experimental finding that crystals under large tensile strains are more stable than crystals under compressive strains. It is one of the strengths of the PFC that these nonlinear effects, both due to elasticity and large interfacial perturbations, can be captured for a system that evolves on diffusive time scales.

As the system size expands toward the most unstable mode, the interface displays sharper valleys and broader peaks. This trend continues until the grooves become too sharp and deep and dislocations are emitted that relieve the highly concentrated stress at valleys. The dislocations propagate toward the unperturbed lower solid-liquid interface as predicted by the classical elasticity theory since this lowers the elastic energy in the solid. Once the dislocations are emitted, the amplitudes of the surface profiles decrease and the grooves become rather rounded as a result of the reduction in the elastic energy. Similar results are found in three dimensions, a snapshot of the interfacial evolution of a body-centered cubic crystal in contact with a liquid is shown in Fig. 8. Dislocations are also emitted at the roots of the grooves just after the islands shown are formed.

V. CONCLUSIONS

We have investigated the interfacial morphology of a uniaxially strained solid that is in contact with liquid using the PFC model. We find that despite the diffusional dynamics employed in the PFC the elastic field induced by the interfacial instability is in quantitative agreement with continuum theory. This suggests that for PFC parameters studied in this paper the elastic field relaxes much faster than the density field and the solid is in mechanical equilibrium on diffusive time scales. The elastic relaxation and diffusion processes are associated with the nonconserved dynamics of the amplitudes of density waves and the conserved dynamics of the density, respectively, which is shown explicitly in recent amplitude equation derivations.

The PFC agrees quantitatively with classical linear stability theory in the early stages of the evolution of the instability, when the wavelengths of the perturbations are larger than the interface thickness and the strains are small. Our results show that when the strains are large, however, nonlinear elasticity gives rise to an asymmetry of the critical wavenumber between tensile and compressive strains when the surface perturbation is small. This dependence of stability of the film surface on the sign of the applied strain has been observed in experiments for SiGe alloys in which large strains are attainable before dislocations form. At the later stages of the evolution, when the surface amplitudes are large, these nonlinear elastic effects give rise to interfacial morphologies that depend on the sign of the applied strain, especially in those regions of large strains. These large strain regions follow from the interfacial morphology and thus can be expected even when the applied strain is small.

The interface thickness, generally assumed to be zero in classical theory, plays an important role in the evolution of the stress-induced instability when the wavelength is comparable to the interface thickness. Past experiments and numerical simulations are in good agreement with classical theory on the macroscopic length scale where the sharp interface assumption of classical theory is a good approximation. However, at the nanoscale, the wavelength of the instability is on the order of the interface thickness, the sharp interface assumption is no longer valid. The PFC predicts a lower value of the critical wavenumber than that obtained from classical theory, which suggests a more stable film surface. It is because the elastic field due to perturbations decays from the surface at the length scale equal to the wavelength of perturbations, and the elastic constants are smaller in the interface region than that in the solid. Therefore a reduction in the elastic energy of the solid-liquid system due to the interface thickness is greater when the ratio of the interface thickness to the wavelength of perturbation is larger.

ACKNOWLEDGMENTS

This research was supported by the NSF DMI. We thank Zhi-Feng Huang, Ken Elder, and Katsuyo Thornton for many valuable discussions.

APPENDIX A: POISSON'S RATIO

For a solid under compression in the $\hat{x}$ direction, the density field can be written in the form analogous to Eq. (8) with the principal reciprocal lattice vectors

$$\vec{K}_1 = (1+\delta k_x)\hat{i},$$

$$\vec{K}_2 = -\frac{1}{2}(1+\delta k_x)\hat{i} - \frac{\sqrt{3}}{2}(1+\delta k_y)\hat{j},$$

$$\vec{K}_3 = -\frac{1}{2}(1+\delta k_x)\hat{i} + \frac{\sqrt{3}}{2}(1+\delta k_y)\hat{j},$$

$$\vec{K}_4 = -(1+\delta k_x)\hat{i},$$

$$\vec{K}_5 = \frac{1}{2}(1+\delta k_x)\hat{i} + \frac{\sqrt{3}}{2}(1+\delta k_y)\hat{j},$$

$$\vec{K}_6 = \frac{1}{2}(1+\delta k_x)\hat{i} - \frac{\sqrt{3}}{2}(1+\delta k_y)\hat{j}, \tag{A1}$$

which yields

$$\psi(\vec{r}) = \bar{\psi} + 2A\left\{\cos[(1+\delta k_x)x] + 2\cos\left(\frac{1+\delta k_x}{2}x\right)\right.$$
$$\left.\times\cos\left[\frac{\sqrt{3}}{2}(1+\delta k_y)y\right]\right\}, \tag{A2}$$

where we assume the amplitudes of density waves are the same for simplicity. To determine the δk_y dependence on the δk_x, we substitute Eq. (A2) into Eq. (5) and minimize the resulting free energy with respect to δk_y, which yields

$$\delta k_y = -1 + \sqrt{1 - \frac{2}{3}\delta k_x - \frac{1}{3}\delta k_x^2}. \tag{A3}$$

Poisson's ratio is

$$\nu = -\frac{\epsilon_{yy}}{\epsilon_{xx}} = -\frac{[1/(1+\delta k_y)-1]}{[1/(1+\delta k_x)-1]} \approx -\frac{\delta k_y}{\delta k_x}. \tag{A4}$$

For small strains, $\delta k_x \ll 1$, δk_y is equal to approximately $-\frac{1}{3}\delta k_x$ and $\nu \approx \frac{1}{3}$.

The same calculation is repeated for hexagons lattices under compression in the $\hat{y}$ direction to check the isotropy of hexagonal lattices. We find

$$\delta k_x = -1 + \sqrt{1 - \frac{2}{3}\delta k_y - \frac{1}{3}\delta k_y^2} \tag{A5}$$

which is the same expression as in Eq. (A3) and hence the same Poisson's ratio regardless of crystal orientation. The amplitude and free-energy density are

$$A = -\frac{1}{5}\bar{\psi} + \frac{1}{15}\sqrt{15\delta - 36\bar{\psi}^2 - 5\alpha}, \tag{A6}$$

$$f_s = -(\delta-1)\frac{\bar{\psi}^2}{2} + \frac{\bar{\psi}^4}{4} - 3\delta A^2 + 9\bar{\psi}^2 A^2$$
$$+ 12\bar{\psi}A^3 + \frac{45}{2}A^4 + \alpha A^2, \tag{A7}$$

where

$$\alpha = 4\delta k_x^2 + 4\delta k_x^3 + \delta k_x^4. \tag{A8}$$

APPENDIX B: ASYMMETRIC ELASTIC ENERGY

For small strains, $\delta k_x \ll 1$, Eq. (A6) can be expanded as

$$A \approx -\frac{1}{5}\bar{\psi} + \frac{1}{15}\sqrt{15\delta - 36\bar{\psi}^2}\left(1 - \frac{5\alpha}{30\delta - 72\bar{\psi}^2}\right)$$
$$= A_o - \frac{1}{6}(15\delta - 36\bar{\psi}^2)^{-1/2}\alpha, \tag{B1}$$

where A_o is the amplitude of the stress-free solid as shown in Eq. (9). Substituting Eq. (B1) into Eq. (A7), we obtain

$$f_s = f_s^o + 4(A_o)^2\delta k_x^2 + 4(A_o)^2\delta k_x^3 + O(\delta k_x^4),$$

$$\mathcal{E} \equiv f_s - f_s^o \approx 4(A_o)^2\delta k_x^2 + 4(A_o)^2\delta k_x^3, \tag{B2}$$

where f_o is the free-energy density of the stress-free solid as shown in Eq. (5). The odd order terms of δk_x in the free-energy density expression give rise to the asymmetry of the free energy under tensile and compressive strains.

[1] R. J. Asaro and W. A. Tiller, Metall. Trans. **3**, 1789 (1972).
[2] M. A. Grinfeld, Sov. Phys. Dokl. **31**, 831 (1986).
[3] D. J. Srolovitz, Acta Metall. **37**, 621 (1989).
[4] B. J. Spencer, P. W. Voorhees, and S. H. Davis, Phys. Rev. Lett. **67**, 3696 (1991).
[5] B. J. Spencer, P. W. Voorhees, and S. H. Davis, J. Appl. Phys. **73**, 4955 (1993).
[6] Z.-F. Huang and K. R. Elder, Phys. Rev. Lett. **101**, 158701 (2008).
[7] W. H. Yang and D. J. Srolovitz, Phys. Rev. Lett. **71**, 1593 (1993).
[8] P. Nozières, J. Phys. I **3**, 681 (1993).
[9] B. J. Spencer, S. H. Davis, and P. W. Voorhees, Phys. Rev. B **47**, 9760 (1993).
[10] B. J. Spencer and D. I. Meiron, Acta Metall. **42**, 3629 (1994).
[11] K. Kassner and C. Misbah, EPL **28**, 245 (1994).
[12] D. E. Jesson, S. J. Pennycook, J.-M. Baribeau, and D. C. Houghton, Phys. Rev. Lett. **71**, 1744 (1993).
[13] Y. H. Xie, G. H. Gilmer, C. Roland, P. J. Silverman, S. K. Buratto, J. Y. Cheng, E. A. Fitzgerald, A. R. Kortan, S. Schuppler, M. A. Marcus, and P. H. Citrin, Phys. Rev. Lett. **73**, 3006 (1994).
[14] B. J. Spencer, P. W. Voorhees, and J. Tersoff, Phys. Rev. Lett. **84**, 2449 (2000).
[15] B. J. Spencer, P. W. Voorhees, and J. Tersoff, Phys. Rev. B **64**, 235318 (2001).
[16] J. Müller and M. Grant, Phys. Rev. Lett. **82**, 1736 (1999).
[17] K. Kassner and C. Misbah, EPL **46**, 217 (1999).
[18] K. Kassner, C. Misbah, J. Müller, J. Kappey, and P. Kohlert, Phys. Rev. E **63**, 036117 (2001).
[19] M. Haataja, J. Müller, A. D. Rutenberg, and M. Grant, Phys. Rev. B **65**, 165414 (2002).
[20] K. R. Elder, M. Katakowski, M. Haataja, and M. Grant, Phys. Rev. Lett. **88**, 245701 (2002).
[21] K. R. Elder and M. Grant, Phys. Rev. E **70**, 051605 (2004).
[22] K. R. Elder, N. Provatas, J. Berry, P. Stefanovic, and M. Grant, Phys. Rev. B **75**, 064107 (2007).
[23] N. Provatas, J. A. Dantzig, B. Athreya, P. Chan, P. Stefanovic, N. Goldenfeld, and K. R. Elder, JOM **59**, 83 (2007).
[24] K.-A. Wu and A. Karma, Phys. Rev. B **76**, 184107 (2007).
[25] P. Stefanovic, M. Haataja, and N. Provatas, Phys. Rev. Lett. **96**, 225504 (2006).
[26] M. P. Gururajan and T. A. Abinandanan (unpublished).
[27] D. H. Yeon, Z.-F. Huang, K. R. Elder, and K. Thornton, Philos. Mag. (to be published).